Chapter 3

Construction of finite-frequency kernels using adjoint methods

Note

This chapter contains excerpts from "Seismic tomography, adjoint methods, time reversal, and banana-doughnut kernels," by Jeroen Tromp, Carl Tape, and Qinya Liu. My primary contribution to this study was to adapt a 2D SEM wave propagation code to construct finite-frequency kernels. In a series of numerical experiements, I illustrated the formation of finite-frequency sensitivity kernels via the interaction between a forward wavefield ($\mathbf{s}$), propagating from source to receiver, with an adjoint wavefield ($\mathbf{s}^\dagger$), propagating from receiver to source. In this chapter, I have included some additional figures to complement those in *Tromp et al.* (2005).

3.1 Kernel Gallery

Expressions for seisitivity kernels for a α-β-ρ parameterization of compressional wave speed (α), shear wave speed (β), and density (ρ) are given by *Tromp et al.* (2005, Eq. 51):

$$\begin{aligned}
\bar{K}_{\rho(\alpha\beta)} &= \bar{K}_{\rho(\kappa\mu)} + \bar{K}_{\kappa(\mu\rho)} + \bar{K}_{\mu(\kappa\rho)}, \\
\bar{K}_{\beta(\alpha\rho)} &= 2\left(\bar{K}_{\mu(\kappa\rho)} - \frac{4}{3}\frac{\mu}{\kappa}\bar{K}_{\kappa(\mu\rho)}\right), \\
\bar{K}_{\alpha(\beta\rho)} &= 2\left(1 + \frac{4}{3}\frac{\mu}{\kappa}\right)\bar{K}_{\kappa(\mu\rho)} \;. \qquad (3.1)
\end{aligned}$$

Appendix B shows similar expressions for parameterizations in κ-μ-ρ and c-β-ρ.

We use a two-dimensional (2D) elastic wave propagation code to illustrate the construction of sensitivity kernels using the adjoint methodology discussed in this paper. Each kernel is based upon the interaction between a regular wavefield $\mathbf{s}$ and an adjoint wavefield $\mathbf{s}^\dagger$. Changing the adjoint source $\mathbf{f}^\dagger$ results in a different adjoint field $\mathbf{s}^\dagger$ and, hence, different kernels. For example, we can use the residuals between the data and the synthetics as the waveform adjoint source to construct misfit kernels, or we can use the synthetic velocity field as the traveltime adjoint source to construct banana-doughnut kernels. In this section we present examples of finite-frequency traveltime kernels.

3.1.1 Model setup

We simulate 2D elastic wave propagation using a spectral-element method, which combines the flexible spatial parameterization of finite-element methods with the accuracy of pseudospectral methods (e.g., *Komatitsch and Tromp*, 1999). The source-receiver geometry and the various SH and P-SV body-wave arrivals are illustrated in Figure 3.1. The top boundary is a free surface, whereas the remaining three boundaries are absorbing to mimic a half space. The model extends 200 km in width and 80 km in depth, and is homogeneous with density $\rho = 2600$ kg m^{-3}, bulk modulus $\kappa = 5.20 \times 10^{10}$ Pa, and shear modulus $\mu = 2.66 \times 10^{10}$ Pa; these values correspond to a compressional wave speed of $\alpha = 5800$ m s^{-1} and a shear wave speed of $\beta = 3199$ m s^{-1}. We use a simple one-way treatment for the implementation of the absorbing boundary conditions (*Komatitsch and Tromp*, 1999). For pedagogical reasons, both the source and the receiver are located at a depth of 40 km to generate direct and surface reflected waves, leading to a variety of interesting phases and associated kernels.

The source-time function used in the simulations is a Gaussian of the form

$$h(t) = (-2\alpha^3/\sqrt{\pi})\ (t - t_0)\ \exp[-\alpha^2 (t - t_0)^2], \tag{3.2}$$

where $t_0 = 8.0$ s, $\alpha = 2\tau_0/\tau$, $\tau_0 = 2.628$ s, and τ is the duration of $h(t)$ (e.g., Figure 3.2a). The source duration is $\tau = 4.0$ s in each example, with the exception of Figure 1.1, where we also used $\tau = 8.0$ s. In each simulation the source is applied in the x and y directions to generate both P-SV and SH motions (which are of course completely decoupled). Changing the orientation of the source results in different sensitivity kernels.

3.1.2 Banana-doughnut kernels

Banana-doughnut traveltime kernels are constructed by using the time-reversed velocity field at one particular receiver as the adjoint source. Kernels calculated in this manner may be compared with the finite-frequency kernels presented in recent studies using ray-based methods (e.g., *Hung et al.*, 2000). As discussed earlier, the construction of each kernel is based on the interaction between the time-reversed regular field and the adjoint field; hence the "interaction field" can be thought of as propagating from the receiver to the source in reverse time from $t = T$ to $t = 0$.

SH waves

We begin with the simplest case, the SH wavefield. The experimental setup is depicted in Figure 3.1. Because both the source and the receiver are located at depth, there are two possible arrivals, which we label S and SS. The source-time function used to generate the regular wavefield is shown in Figure 3.2a, and the associated seismogram with distinct S and SS arrivals is displayed in Figure 3.2b. Figure 3.3 illustrates the construction of the $\bar{K}_{\beta(\alpha\rho)}$ kernel from the interaction between the regular field $\mathbf{s}$ and the S adjoint field $\mathbf{s}^{\dagger}$, whose source is shown in Figure 3.2d. Keep in mind that for increasing time t the regular field propagates from the source to the receiver, whereas the adjoint field propagates from the receiver to the source. Marching backward in time from $t = T$, the traveltime adjoint source (located at the receiver) "turns on" at the precise moment that the regular S wavefield passes over it (between Figure 3.3a and 3.3b). At each moment in time the two wavefields are combined via (3.1) to form the "interaction" field, which is integrated to construct the kernel. In other words, the interaction field represents the time-dependent integrand in the kernel definition. Once the regular source is "extinguished," no further contributions are made toward $\bar{K}_{\beta(\alpha\rho)}$. Note that $\bar{K}_{\beta(\alpha\rho)}$ is cigar-shaped rather than banana-shaped because the model is homogeneous, and there is no doughnut hole because we are dealing with 2D rather than 3D kernels. We refer to this example as SH_{S}, where SH designates participation of only the y-component of the wavefields, and the subscript S denotes the phase that is being reversed. The pulse is tapered within the time window w_r using a Welch window (*Press et al.*, 1994).

Figures 3.4 and 3.5 show the effect of reversing different time windows of the synthetic velocity field. Reversing the SS pulse gives a kernel in the shape of a "folded-over cigar" (Figure 3.5f). The ellipse surrounding the source and receiver represents SS scatterers with comparable traveltimes to the SS wave reflected at the surface. Reversing the entire waveform (i.e., both pulses) illuminates the sensitivity regions of both S and SS (Figure 3.5gh).

Figure 3.6 shows all six kernels for the $\mathrm{SH_S}$ scenario. These kernels are constructed simultaneously via the process illustrated in Figure 3.3 for $\bar{K}_{\beta(\alpha\rho)}$. Notice that the relative amplitudes of the kernels are consistent with what is expected from the relationships in (3.1). For example, since $\bar{K}_{\kappa(\mu\rho)} = 0$ and $\bar{K}_{\mu(\kappa\rho)} \approx -\bar{K}_{\rho(\kappa\mu)}$, we see that $\bar{K}_{\rho(\alpha\beta)} = \bar{K}_{\mu(\kappa\rho)} + \bar{K}_{\kappa(\mu\rho)} + \bar{K}_{\rho(\kappa\mu)}$ is very weak. Note that for SH waves we have $\bar{K}_{\beta(\alpha\rho)} = 2\,\bar{K}_{\mu(\kappa\rho)}$.

Figure 1.1 (Chapter 1) illustrates the effect of changing the source duration, τ in (3.2), on the kernels. We see that the width of the kernel shrinks at higher frequencies. We expect this since in the limit of infinite frequency the kernel should collapse onto the ray path. Note that the amplitude of the kernel increases with increasing frequency. This frequency dependence was illustrated by *Hung et al.* (2000) using a different technique to construct the kernels. Cross sections of the kernels (Figure 1.1d) help to highlight the Fresnel zones. In the case of the $\mathrm{SH_S}$ β-kernel, the broad, low-sensitivity red zone represents the first Fresnel zone, whereas the sidelobes defined by the narrow, high-sensitivity green zone correspond to the second Fresnel zone (e.g., *Hung et al.*, 2000).

P-SV waves

The P-SV wavefield is more complicated than the SH wavefield (Figure 3.1), and even in the homogeneous case Rayleigh waves arise through interactions at the free surface. Figure 3.7 illustrates the construction of the P-SV adjoint source for the PS+SP arrival, and Figures 3.8 and 3.9 show the corresponding formation of the $\bar{K}_{\rho(\alpha\beta)}$, $\bar{K}_{\alpha(\beta\rho)}$, and $\bar{K}_{\beta(\alpha\rho)}$ kernels.

Notice how the interactions $\mathrm{SP{\sim}P^\dagger}$ and $\mathrm{PS{\sim}S^\dagger}$ form the right portion of the sensitivity kernel, e.g., at $t = 32.0$ s (Figure 3.8b), whereas the left portion results from the interactions $\mathrm{P{\sim}SP^\dagger}$ and $\mathrm{S{\sim}PS^\dagger}$, e.g., at $t = 16.0$ s (Figure 3.8d). This can be deduced by matching up the portions of the regular and adjoint wavefields that are contributing to the interaction field. These interactions "paint" the resultant sensitivity kernel.

Figure 3.10 shows all nine kernels for the $\mathrm{P\text{-}SV_{PS+SP}}$ scenario. We have included the c-β-ρ parameterization, where c is bulk sound speed, in addition to the κ-μ-ρ and α-β-ρ cases. These expressions are derived in Appendix B.

Figure 3.11 shows the effect of reversing four distinct time windows of the P-SV synthetic velocity field: the P, PP, PS+SP, and SS arrivals. In Figure 3.11b we see that the α-kernel for P-SV$_{\mathrm{P}}$ is wider than the β-kernel for SH$_{\mathrm{S}}$ (Figure 3.5c) for the same source period. This is due to the relatively longer wavelengths of the P waves: $\lambda_\alpha = \alpha T > \lambda_\beta = \beta T$. Figures 3.11c-f illustrate examples of α and β kernels for the P-SV$_{\mathrm{PP}}$, P-SV$_{\mathrm{PS+SP}}$, and P-SV$_{\mathrm{SS}}$ scenarios. Note that, as expected, the α-kernel for the SS wave (Figure 3.11e) is insignificant relative to the β-kernel (Figure 3.11f).

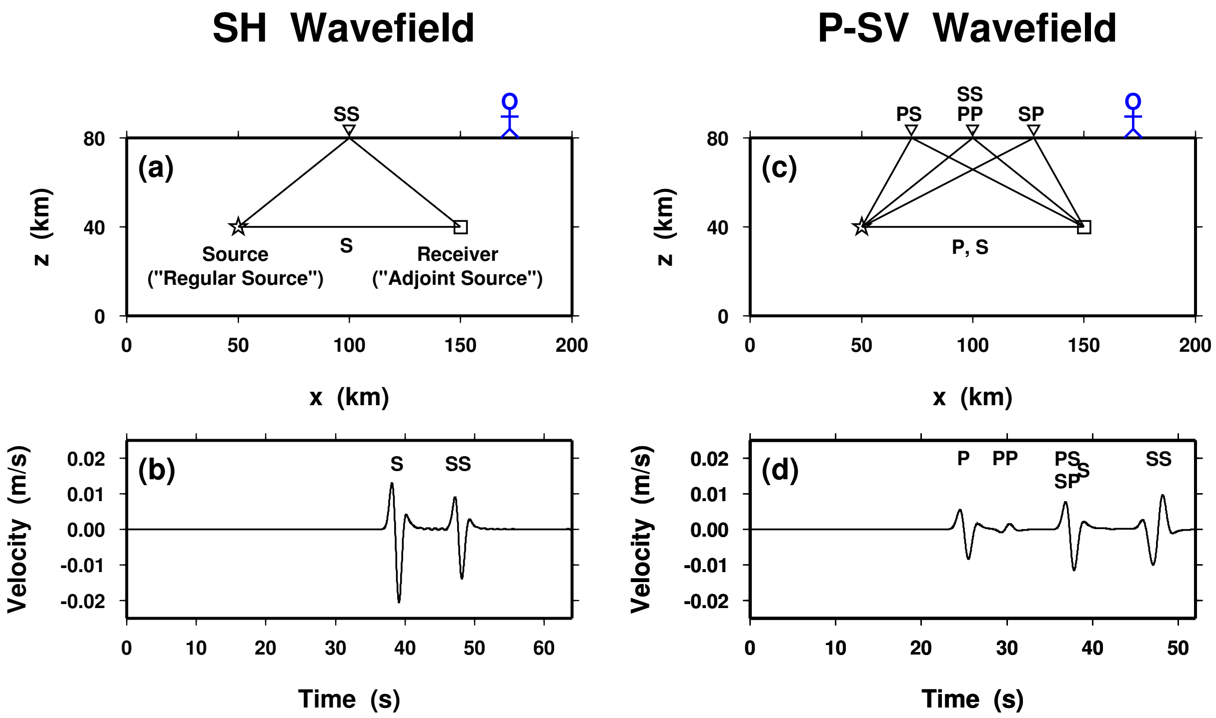

Figure 3.1: Sketch of the 2D model dimensions and the source-receiver geometry (after *Tromp et al.*, 2005, Figure 1). The solid line denotes a free surface, whereas dashed lines are absorbing boundaries. The source is indicated by the $\star$ and the receiver by the $\square$. Left: The two possible ray paths for the SH wavefield are labeled S and SS. The $\bigtriangledown$ denotes the SS bounce point. Right: The possible body-wave ray paths for the P-SV wavefield. The ray paths are based on a homogeneous model.

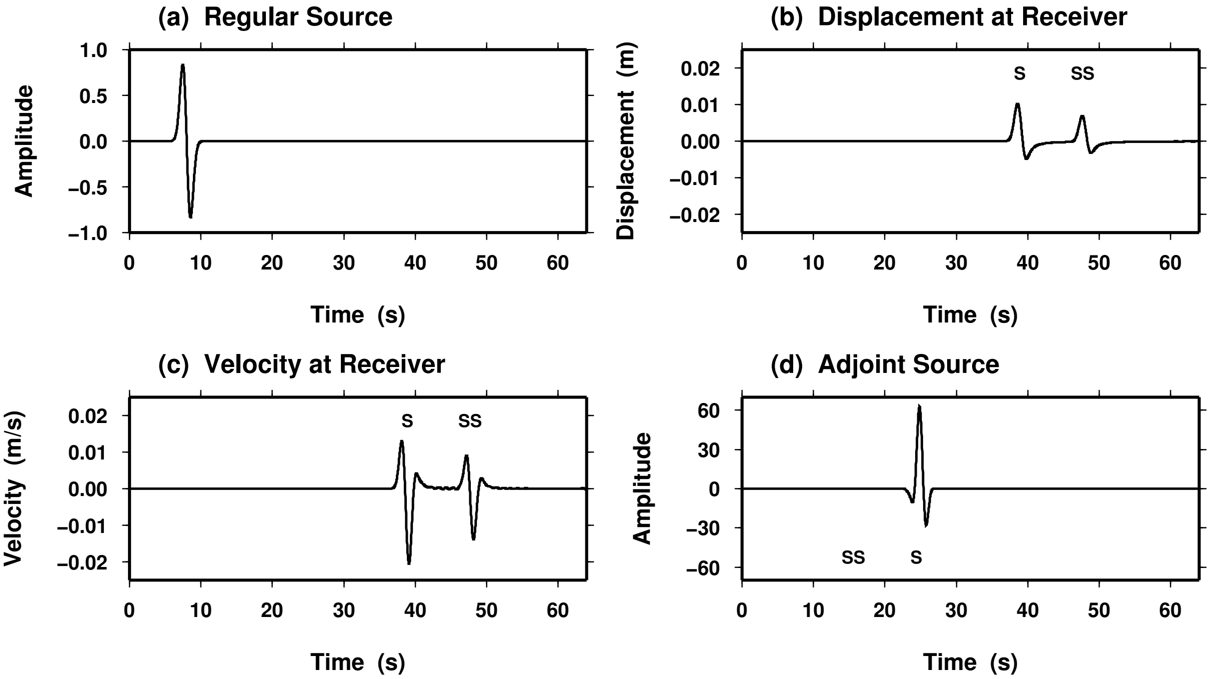

Figure 3.2: Construction of the adjoint source-time function used in calculating SH banana-doughnut kernels (*Tromp et al.*, 2005, Figure 2). All traces represent the y-component. (a) Source for the regular wavefield. (b) Regular seismogram recorded at the receiver. (c) Velocity seismogram at the receiver. (d) Source for the adjoint wavefield constructed by time-reversing (c) and Welch tapering the S arrival. Note that this includes the normalization factor $M_{\mathrm{T}} \leq 0$ defined in *Tromp et al.* (2005).

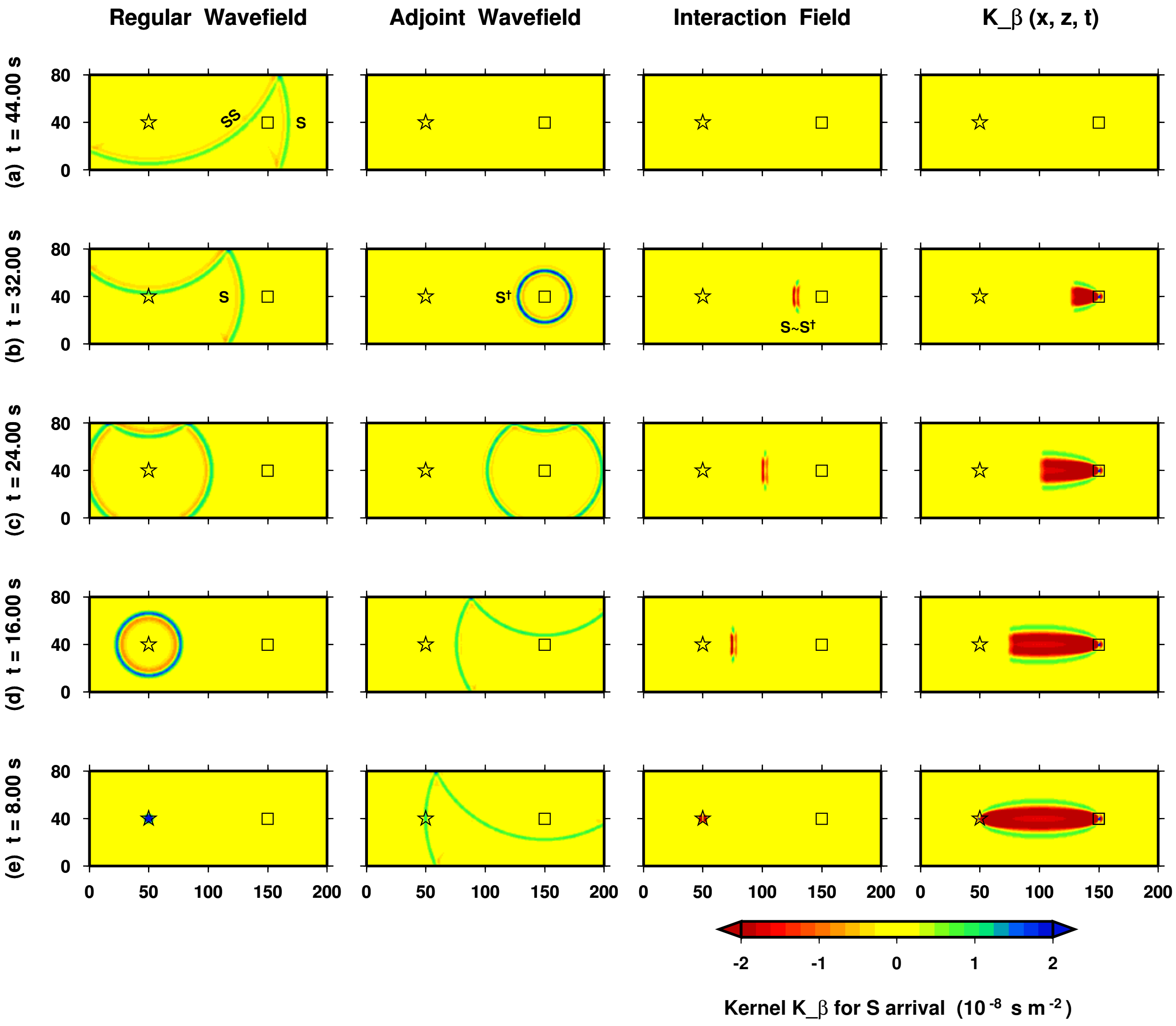

Figure 3.3: Sequence of interactions between the regular and adjoint SH wavefields during the construction of the banana-doughnut kernel $\bar{K}_{\beta(\alpha\rho)}$ (*Tromp et al.*, 2005, Figure 3). This particular $\bar{K}_{\beta(\alpha\rho)}$ kernel is for $\mathrm{SH_S}$, i.e., the SH β–kernel obtained by time-reversing the S arrival. The regular and adjoint sources are shown in Figure 3.2; the model is a homogeneous half space. Each row represents an instantaneous interaction between the regular and adjoint fields. From the left column to the right column are shown the regular field, the adjoint field, the interaction field, and the instantaneous sensitivity to shear velocity perturbations, $\bar{K}_{\beta(\alpha\rho)}$. The $\bar{K}_{\beta(\alpha\rho)}$ kernel is constructed by integrating the interaction field, shown in the third column, over time. (a) At this point in time there is no interaction between the regular field and the adjoint field, since the S wave has yet to reach the receiver. (b) Adjoint wavefield "lights up" as the regular wavefield S phase passes over the receiver (traveling toward the source in reverse time). The label S$\sim$S† indicates interaction between the regular and adjoint S waves, respectively. (c)–(d) The sensitivity kernel forms via the interaction between the regular and adjoint wavefields. (e) Time of regular source initiation, before which no interaction occurs. The source is labeled by the $\star$ and the receiver by the $\square$.

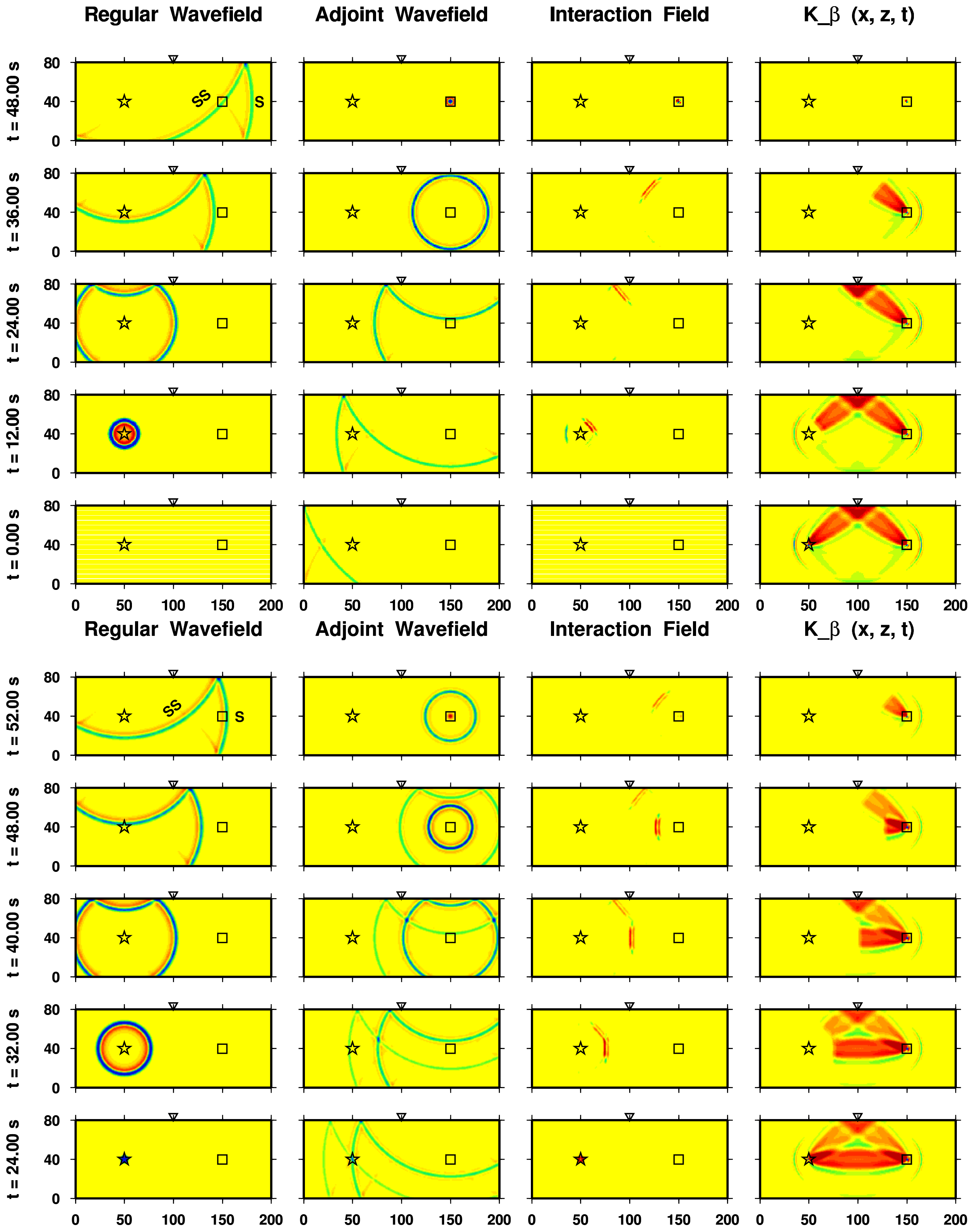

Figure 3.4: Same as Figure 3.3, but here we have time-reversed the SS arrival (top) and the entire record (bottom).

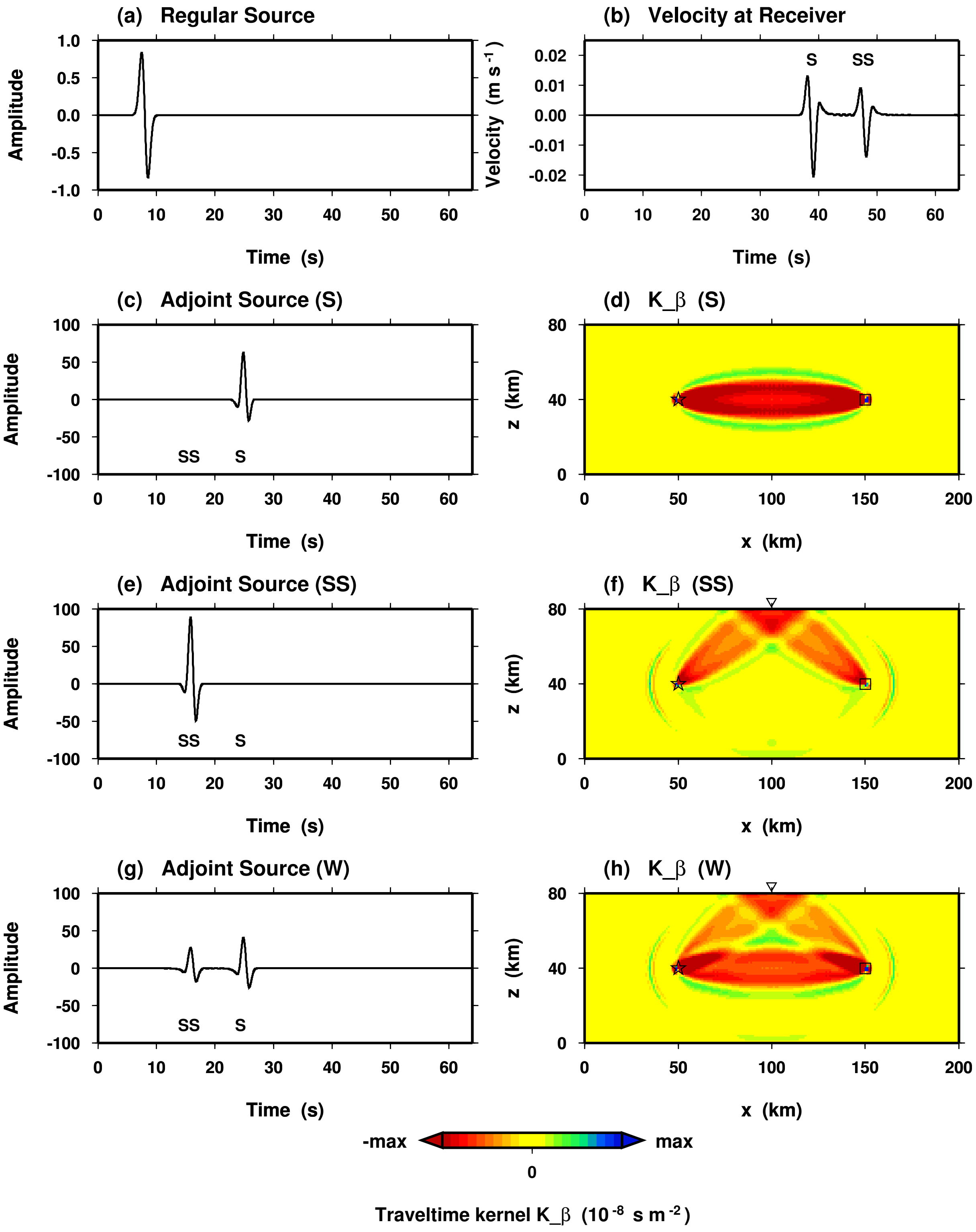

Figure 3.5: The effect of time window selection on sensitivity kernels, using $\bar{K}_{\beta(\alpha\rho)}$ (SH) as an example (after *Tromp et al.*, 2005, Figure 5). (a) Source for the regular wavefield. (b) Velocity recorded at the receiver showing the arrivals S and SS. (c) Adjoint source for SH$_{\mathrm{S}}$, constructed by time-reversing S in (b) and normalizing by M_{T} defined in *Tromp et al.* (2005). (d) $\bar{K}_{\beta(\alpha\rho)}$ for reversing S only. (e) Adjoint source for SH$_{\mathrm{SS}}$, constructed by time-reversing SS in (b) and normalizing by M_{T}. (f) $\bar{K}_{\beta(\alpha\rho)}$ for reversing SS only. Each point on the ellipse represents a scattering point for a path with a comparable traveltime to the SS path. The SS bounce point is labeled by the $\bigtriangledown$, the source by the $\star$, and the receiver by the $\Box$.

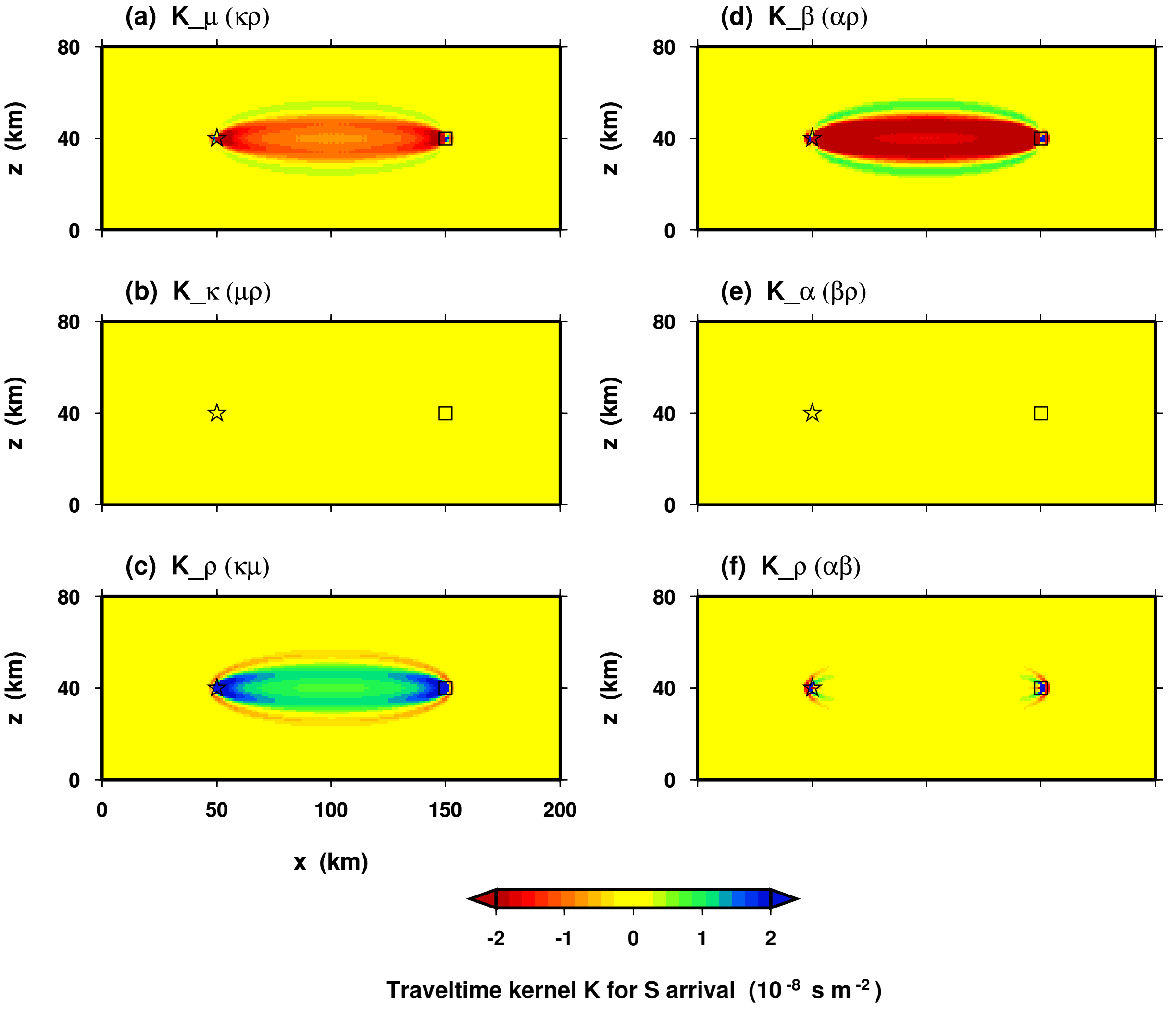

Figure 3.6: The six $\mathrm{SH_S}$ banana-doughnut kernels. Each kernel is constructed simultaneously as shown in Figure 3.3 for $\bar{K}_{\beta(\alpha\rho)}$. Note that $\bar{K}_{\alpha(\beta\rho)} = \bar{K}_{\kappa(\mu\rho)} = 0$, $\bar{K}_{\beta(\alpha\rho)} = 2\bar{K}_{\mu(\kappa\rho)}$, $\bar{K}_{\mu(\kappa\rho)} \approx -\bar{K}_{\rho(\kappa\mu)}$, and $\bar{K}_{\rho(\alpha\beta)} \approx 0$ for SH propagation.

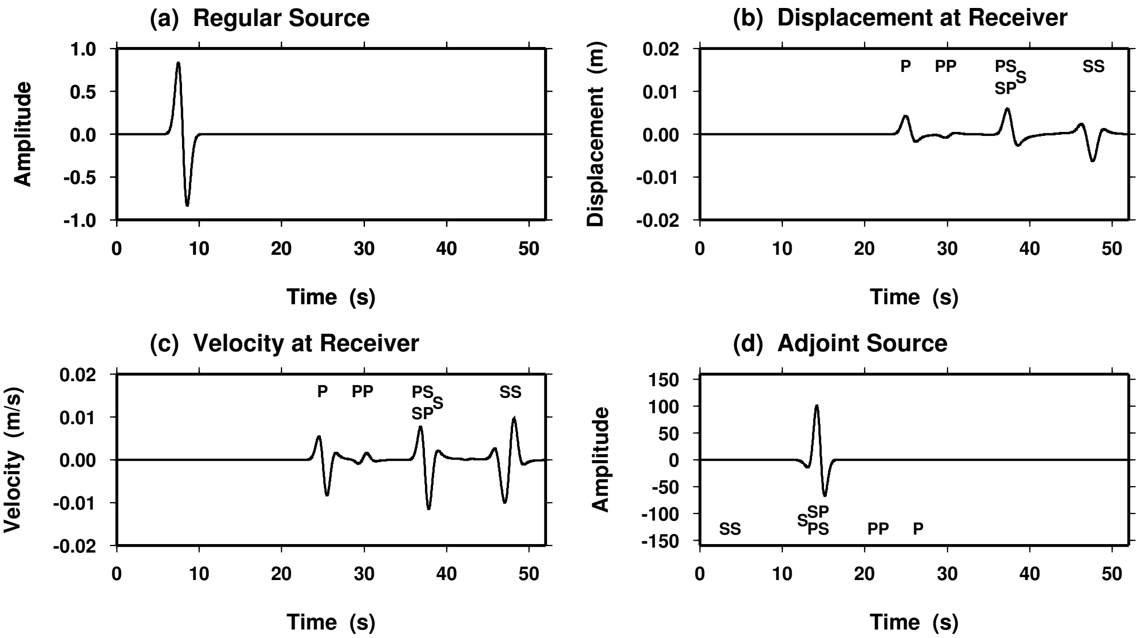

Figure 3.7: Construction of the adjoint source-time function used in calculating P-SV banana-doughnut kernels. (a) Source-time function responsible for the regular wavefield (x-component; the z-component is zero). (b) Regular seismogram (x-component). (c) Velocity seismogram (x-component). (d) Source-time function for the adjoint source constructed by time-reversing (c) and Welch tapering the PS+SP arrival (x-component). Note that this includes the normalization factor M_{T} defined in *Tromp et al.* (2005). This is the source-time function used in Figure 3.8.

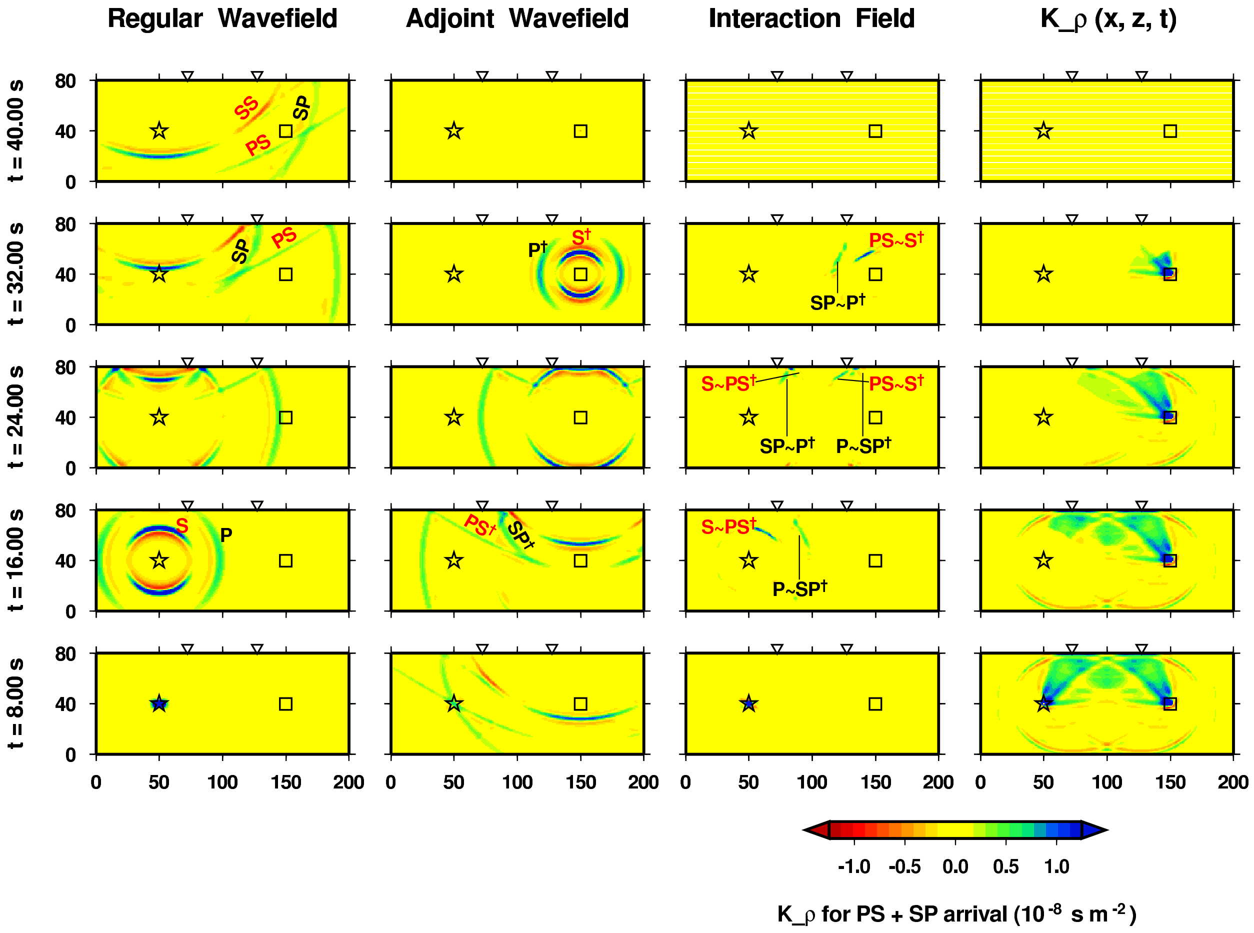

Figure 3.8: Sequence of interactions between the regular and adjoint P-SV wavefields to produce the banana-doughnut kernel $\bar{K}_{\rho(\alpha\beta)}$. This particular $\bar{K}_{\rho(\alpha\beta)}$ is for P-SV$_{\mathrm{PS+SP}}$, i.e., the P-SV ρ-kernel obtained by time-reversing the PS+SP arrival. Given the geometry in Figure 3.1, the SP and PS phases arrive simultaneously, at nearly the same time as the S arrival (Figure 3.7b). The x-z grid in each snapshot is 200 km in width and 80 km in depth. Wavefield snapshots capture the x-component of displacement. We use labels $\star$ for the source, $\square$ for the receiver, and $\bigtriangledown$ for the PS (right) and SP (left) bounce points. See Section 3.1.2 for details, and compare with Figure 3.3. (a) No interaction between the regular and adjoint fields, since the PS+SP phase has yet to reach the receiver. (b) Adjoint wavefield "lights up" as the regular wavefield PS+SP phase, depicted by the X-shaped crossing of the two green wavefields, passes over the receiver (traveling toward the source). (c)–(d) Sensitivity kernel forms via the interaction between the regular and adjoint fields. (e) Time of regular source initiation, before which no interaction occurs.

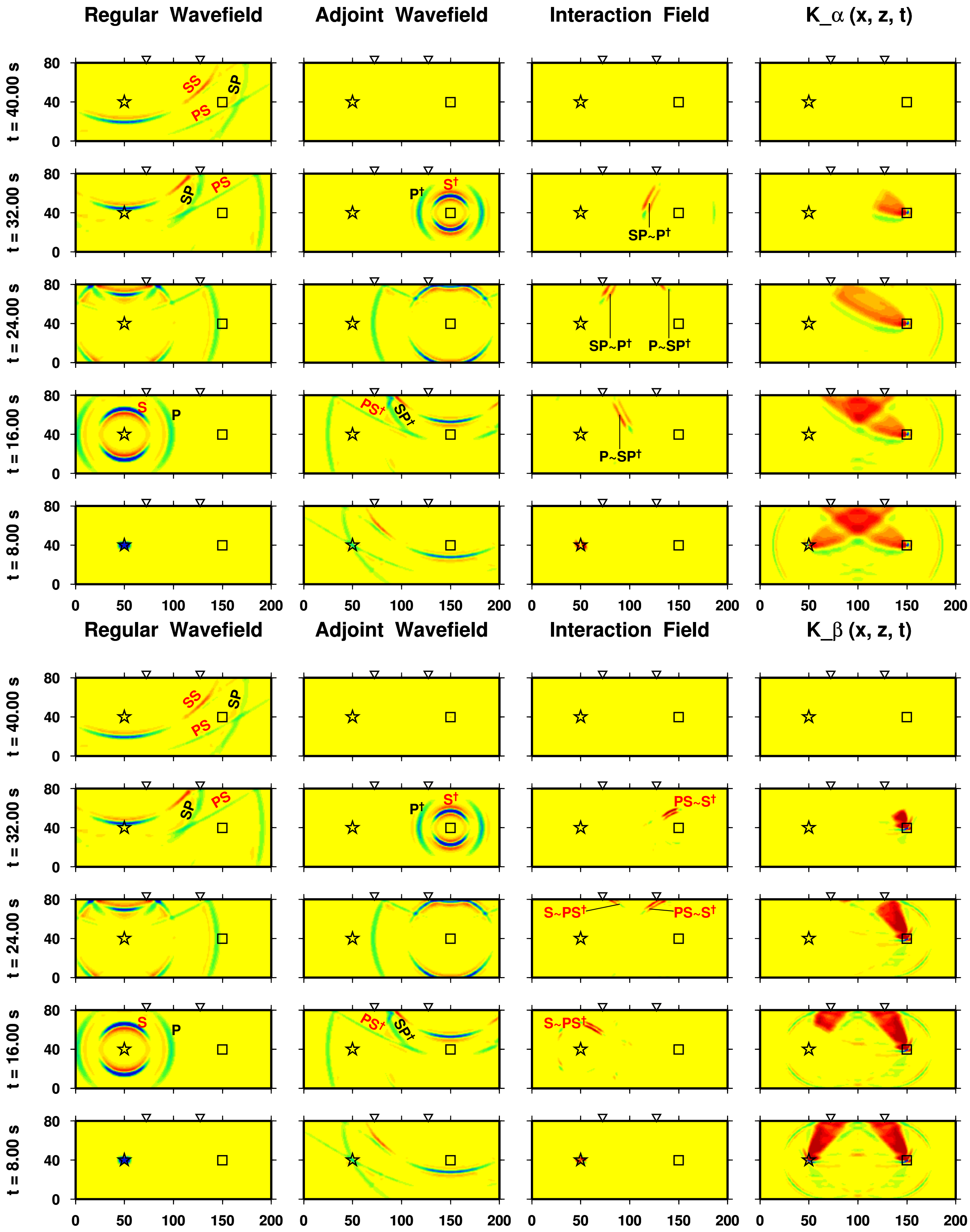

Figure 3.9: Same forward and adjoint wavefields as in Figure 3.8, but here we show the formation of the α-kernel (top) and the β-kernel (bottom).

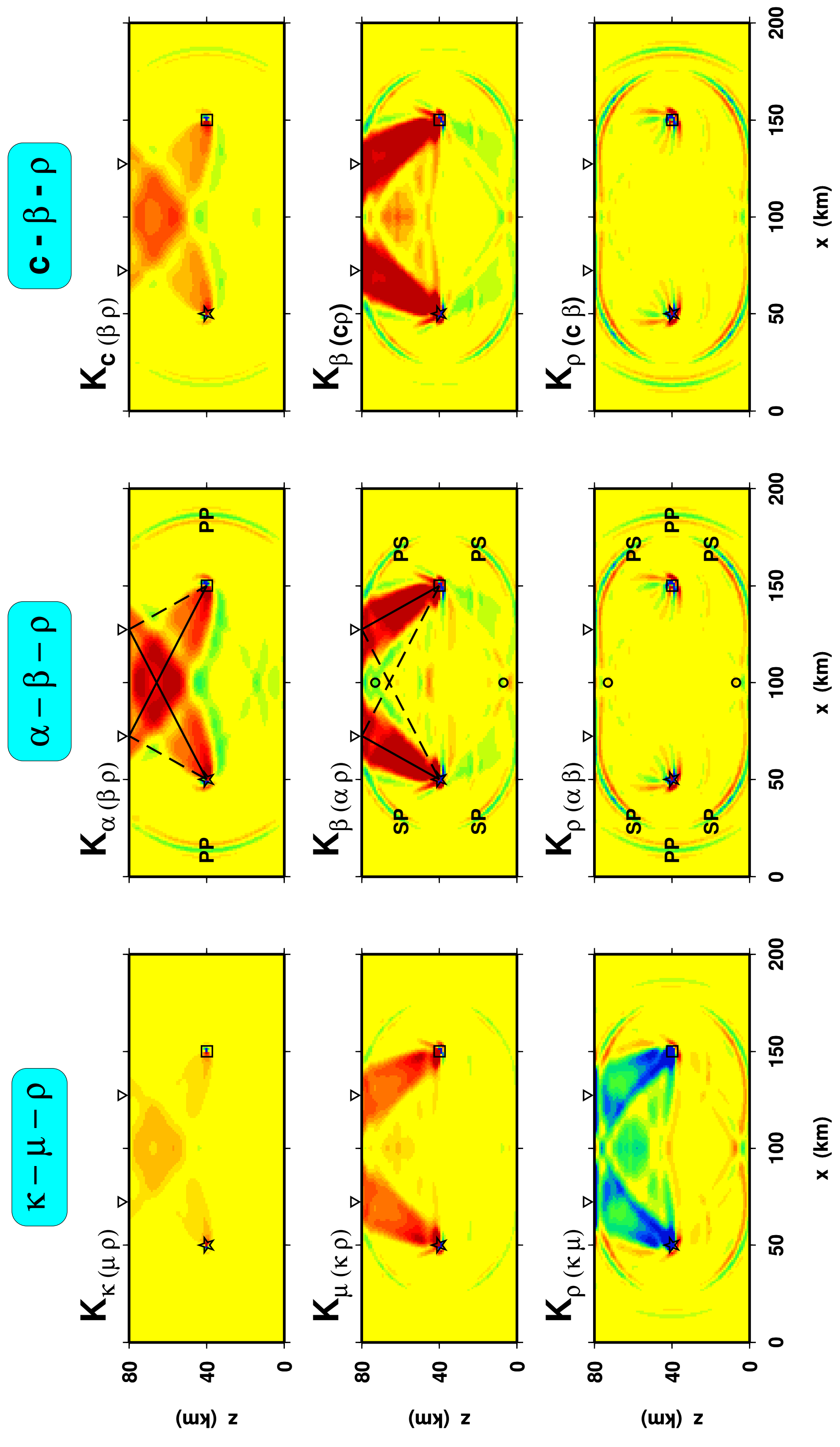

Figure 3.10: P-SV$_{\mathrm{PS+SP}}$ banana-doughnut kernels for three different model parameterizations (see Appendix B). Each kernel is constructed simultaneously, as shown in Figure 3.8. Notice that the predominant shape of the $\bar{K}_{\alpha(\beta\rho)}$ kernel is that of two adjacent, folded-over "cigars," the right one for PS and the left for SP. The labels $\bigtriangledown$ denotes the PS (right) and SP (left) bounce points.

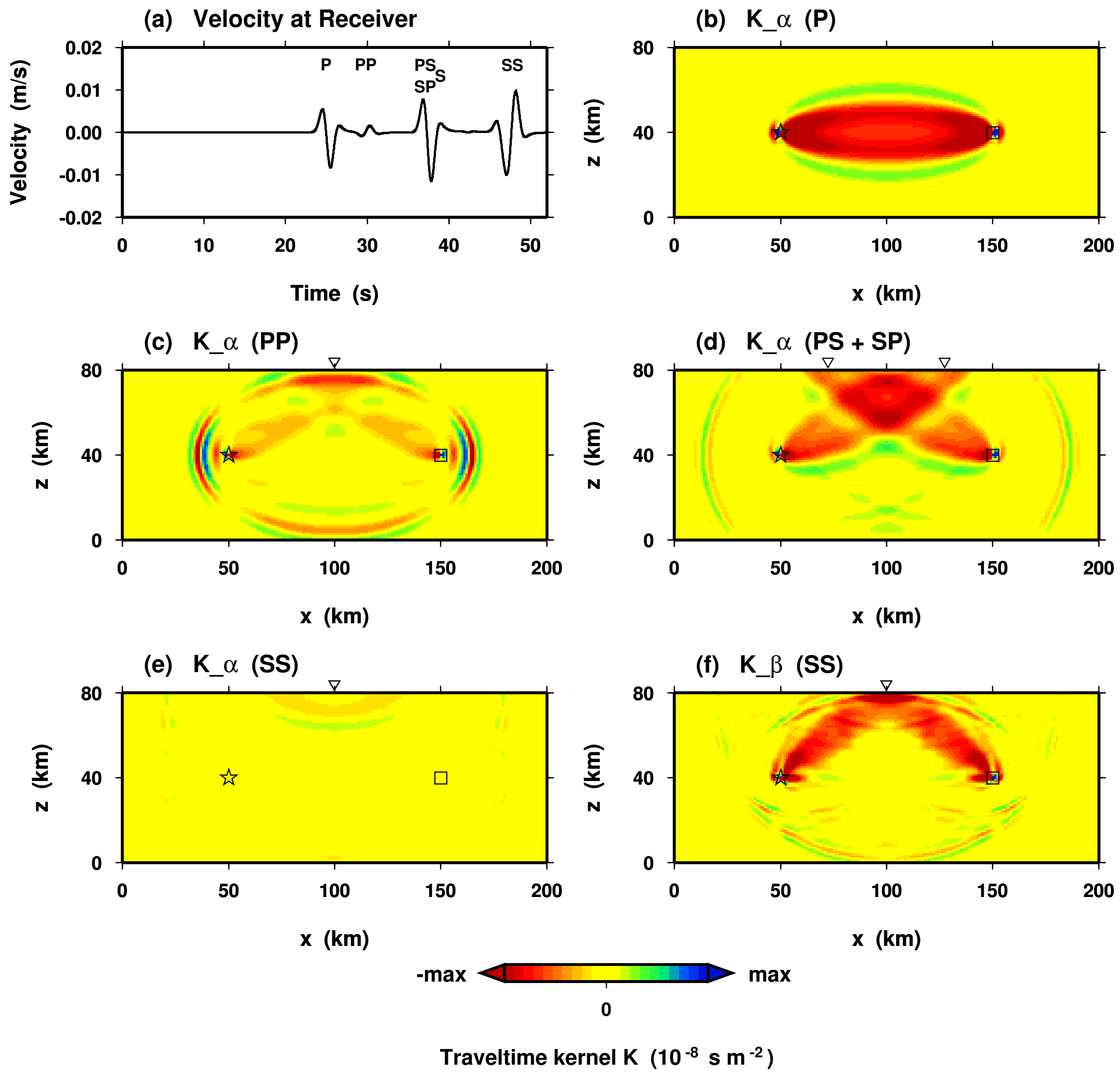

Figure 3.11: The effect of time-window selection on sensitivity kernels, using $\bar{K}_{\alpha(\beta\rho)}$ as an example. See Figure 3.1 for labeling and Section 3.1.2 for details. (a) Velocity recorded at the receiver (x-component) showing the consecutive arrivals of P, PP, PS+SP, and SS. The S phase is expected to arrive nearly simultaneous with PS+SP, but is insignificant on this component. In (b)–(f) we Welch taper one of the pulses and time-reverse it as the adjoint source via the method explained in Figure 3.7. The color scale varies for each plot according to the value "max." (b) $\bar{K}_{\alpha(\beta\rho)}$ for reversing the P arrival ($\text{P-SV}_{\text{P}},\ \max = 1.0$). (c) $\bar{K}_{\alpha(\beta\rho)}$ for reversing the PP arrival ($\text{P-SV}_{\text{PP}},\ \max = 5.0$). (d) $\bar{K}_{\alpha(\beta\rho)}$ for reversing the PS+SP arrival ($\text{P-SV}_{\text{PS+SP}},\ \max = 1.5$). (e) $\bar{K}_{\alpha(\beta\rho)}$ for reversing the SS arrival ($\text{P-SV}_{\text{SS}},\ \max = 2.75$). (f) $\bar{K}_{\beta(\alpha\rho)}$ for reversing the SS arrival ($\text{P-SV}_{\text{SS}},\ \max = 2.75$).